

## Descent and Modification of the Overflow Plume in the Denmark Strait\*

JAMES B. GIRTON<sup>+</sup> AND THOMAS B. SANFORD

*Applied Physics Laboratory and School of Oceanography, University of Washington, Seattle, Washington*

(Manuscript received 23 November 2001, in final form 27 January 2003)

### ABSTRACT

Bulk properties of the Denmark Strait overflow (DSO) plume observed in velocity and hydrography surveys undertaken in 1997 and 1998 are described. Despite the presence of considerable short-term variability, it is found that the pathway and evolution of the plume density anomaly are remarkably steady. Bottom stress measurements show that the pathway of the plume core matches well with a rate of descent controlled by friction. The estimated entrainment rate diagnosed from the rate of plume dilution with distance shows a marked increase in entrainment at approximately 125 km from the sill, leading to a net dilution consistent with previous reports of a doubling of overflow transport measured by current meter arrays. The entrainment rate increase is likely related to the increased topographic slopes in the region, compounded by a decrease in interface stratification as the plume is diluted and enters a denser background.

### 1. Introduction

Dense water from the deep convective regions of the North Atlantic produces a signature of the thermohaline overturning circulation that can be seen as far away as the Pacific and Indian Oceans. The Denmark Strait is one of the most geographically confined locations along this entire “conveyor belt” pathway, carrying approximately half of the dense water formed in the Greenland, Iceland, and Norwegian seas in the form of a near-bottom “overflow” current that descends from the sill depth of 600 m to 2500 m at Cape Farewell (the southern tip of Greenland). The Denmark Strait overflow (DSO), then, is a phenomenon of great importance to researchers interested in understanding the forcing and modifications of the overturning circulation by its individual components, as well as to those interested in monitoring the strength of the circulation on long timescales. In addition, physical processes such as entrainment and bottom drag occur in many similar density currents and overflows, and so knowledge obtained in one is applicable to others.

The ultimate properties of the deep water being formed are determined not only by the direct processes of air–sea interaction that create the initial overflowing

water but also by the mixing with and entrainment of surrounding fluid during the density current’s descent. For this reason, the location and mechanism of entrainment is of vital importance to the ability to simulate deep water changes in ocean models. This combination of localized small-scale physics and global importance presents a particularly difficult challenge for the large-scale numerical models used to study the ocean and global climate. Even with continual improvements in computational power, the resolution needed to simulate overflow processes will not be available on a global scale in the foreseeable future, and so a realistic approach to subgrid-scale parameterization (based on observations) is needed.

### *Past observations of the DSO*

Initial attempts to directly measure the transport through the Denmark Strait met with mixed success (Worthington 1969). It became clear not only that the overflow contains both strong mean and fluctuating components, and can reach instantaneous speeds of  $1.4 \text{ m s}^{-1}$  or more, but also that further progress in mooring design was required. The International Council for the Exploration of the Sea (ICES) “OVERFLOW ’73” expedition (described by Ross 1984; Smith 1976; and hereafter referred to as O73) was far more successful and has remained the most comprehensive set of mooring and hydrographic section data from the Denmark Strait region until very recently. The 37-day mooring deployment in O73 showed that the DSO is highly variable on timescales of 2–5 days but steady over longer periods, with a mean transport of  $2.9 \text{ Sv}$  ( $\text{Sv} \equiv 10^6 \text{ m}^3$

\* Woods Hole Oceanographic Institution Contribution Number 10691.

<sup>+</sup> Current affiliation: Woods Hole Oceanographic Institution, Woods Hole, Massachusetts.

Corresponding author address: James B. Girton, Department of Oceanography, MS 29, WHOI, Woods Hole, MA 02543.  
E-mail: girton@whoi.edu

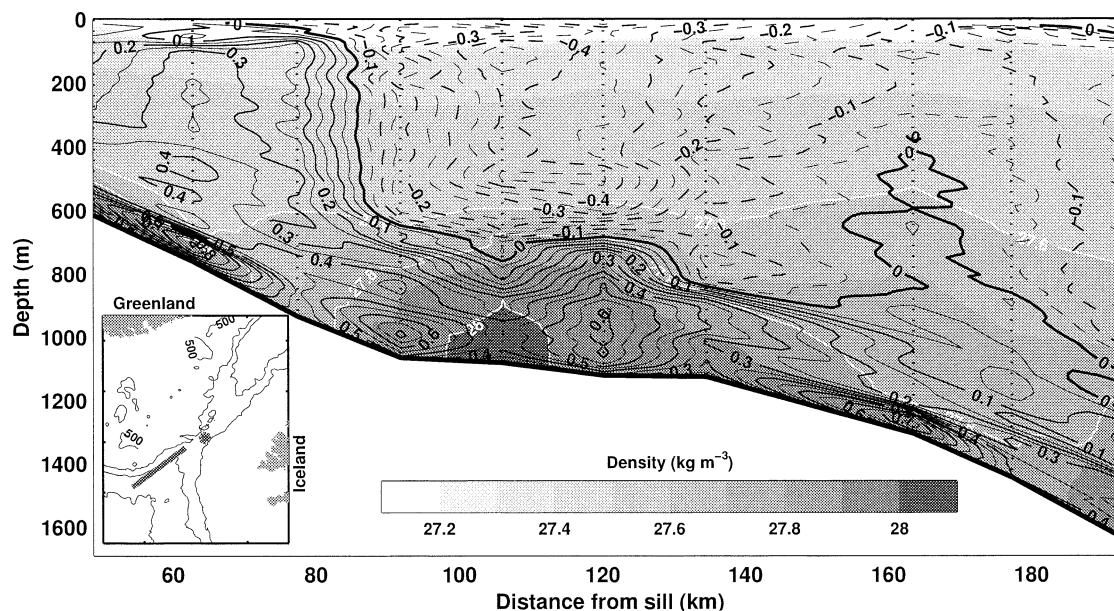


FIG. 1. Overflow velocity and density structure from a section along the approximate path of the plume (location shown by gray line in inset with the sill marked by an asterisk). Profile locations within the section are shown by vertical dotted lines. Density ( $\sigma_\theta$ ) is shaded in grayscale, with the contours for 27.6, 27.8, and 28.0  $\text{kg m}^{-3}$  shown as white lines. Contours of velocity parallel to the section ( $\text{m s}^{-1}$ ) are in black, with dashed contours for negative values (i.e., northeastward flow).

$\text{s}^{-1}$ ) of water colder than  $2^\circ\text{C}$ . Tides play only a small role in the variability, accounting for 2%–10% of the variance in the current meter velocities.

A description of the evolution of the DSO from violent sill flow to (more or less) steady boundary current was not available until the deployment of a set of moorings by the U.K. Lowestoft Laboratories at three sites along the southeast coast of Greenland (Dickson and Brown 1994). These moorings showed the increase in transport of the DSO from 3 to 5 Sv through entrainment during its initial descent as well as subsequent increases to 10 Sv due to the joining of the Iceland–Scotland overflows and eventually to 13 Sv at the southern tip of Greenland after gradual additional mixing.

Another major contribution of the Lowestoft arrays was to confirm a lack of seasonal or interannual overflow variability [as suggested earlier by Aagaard and Malmberg (1978) based on a yearlong current meter deployment]. This led to an apparent contradiction, given the substantial changes in Greenland Sea convective activity on these timescales (Dickson et al. 1996). This has been partially explained by the more gradual transformation process described by Mauritzen (1996) but the question does remain as to what timescale of forcing the overflow will respond.

Since 1993 the Nordic World Ocean Circulation Experiment (WOCE) and European Community-Variability of Exchanges in Northern Seas (EC-VEINS) programs have undertaken a number of cruises to the Denmark Strait sill and nearby regions. Two of these cruises on the Finnish R/V *Aranda* are described by Fristedt et al. (1999) and Rudels et al. (1999). In recent years the

Institut für Meereskunde (IFM), Kiel, has also undertaken a number of cruises with the R/V *Poseidon* and other German vessels to the region, some of which have been briefly described by Krauss and Käse (1998).

## 2. Surveys with expendables

Because of the combined effects of variability on short temporal and spatial scales, we chose to undertake a rapid, high-resolution survey of the Denmark Strait region using ship-lowered (CTD) and expendable (XCP, XCTD) profiling instruments to measure velocity, temperature, and salinity. The expendable instrumentation allowed for faster full-water-column sampling and a greater opportunity to conduct measurements in a region where rough weather often limits ship operations. In addition, the high-resolution velocity measurement of the XCP was particularly desirable for evaluating the influence of bottom boundary layer processes.

Twenty-three XCPs dropped from the *Aranda* in September 1997 gave an initial overview of the speed, structure, and variability of the overflow plume (Girton and Sanford 1999). Bottom-layer velocities as high as  $1.4 \text{ m s}^{-1}$  and as low as  $0.2 \text{ m s}^{-1}$  were observed, with thicknesses ranging from 40 to 400 m. A single section along the overflow's path (Fig. 1) showed a sequence of thick domes of dense water with regions of thin overflow layer in between.

The two accompanying cross-stream sections revealed a dense layer too wide to allow for the interpretation of Fig. 1 as a meandering flow. Instead, the domes

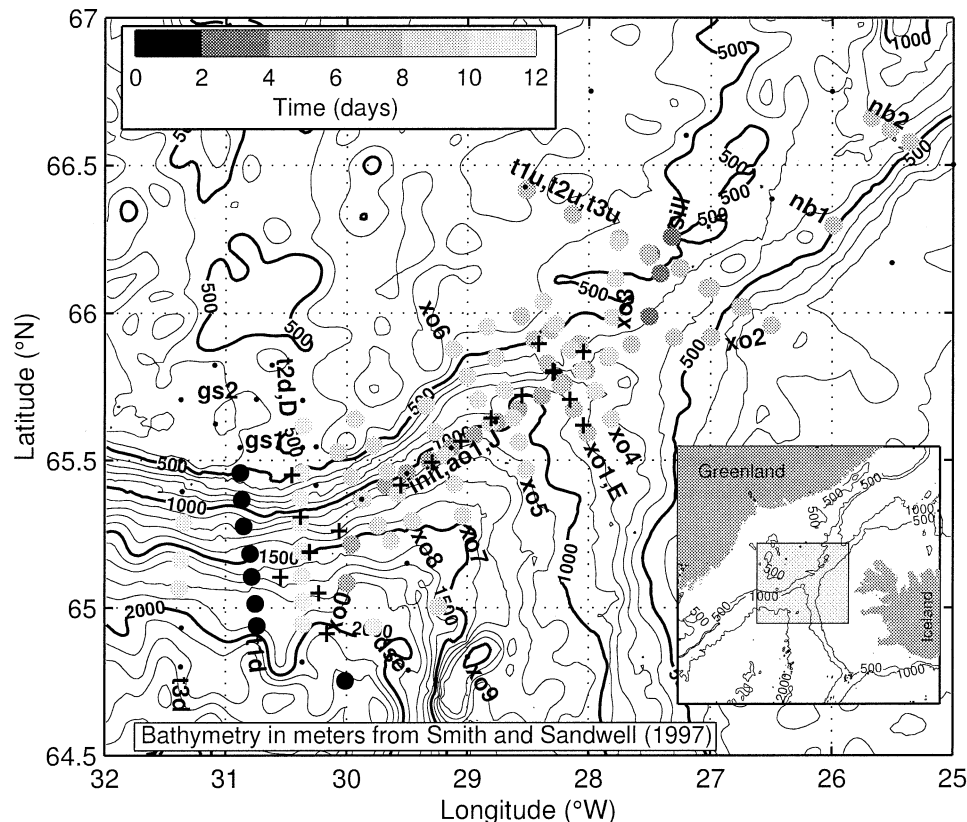


FIG. 2. Locations of XCP drops during *Poseidon* 244 shaded by time elapsed after the first drop at 0558 UTC 15 Sep 1998. Note that the sill section and a few other stations contain overlapping symbols, which may be difficult to separate. Stations without XCPs (i.e., CTD or XCTD only) are shown as small dots. XCP + CTD stations from the 1997 *Aranda* cruise (sections D, E, and J) are indicated by crosses. The inset shows the location of the survey in the Denmark Strait.

appear to represent temporal variability in the form of propagating pulses of overflow water.

A more thorough picture of the structure of the overflow was obtained from a 2-week survey on the *Poseidon* in 1998 (Fig. 2).

The survey consisted primarily of a set of full-water-column sections across the overflow path, and, as such, is well-suited to an examination of the evolution of the plume with distance. Three complete passes were made through the survey region, with a total of 16 cross-plume sections at or downstream of the sill. The pattern and magnitude of variability was similar to that seen in the *Aranda* survey and, in fact, the near-sill transport and variability were almost identical to that measured 25 years earlier by the O73 current meters (Girton et al. 2001).

In this paper, we will restrict our attention to the 87 stations making up the 18 sections across the overflow (including two from 1997). Of these, 68 contained water denser than  $\sigma_\theta = 27.8 \text{ kg m}^{-3}$ . Overall statistics of these profiles are presented in Table 1.

A complete atlas of the *Aranda* and *Poseidon* sections can be found in Girton (2001).

### 3. Methods

#### a. Absolute velocity

Absolute ADCP velocities obtained using differential GPS navigation were used to reference the XCP profiles of relative velocity in the near-surface region of overlap. Figure 3a shows a typical example of the very good match between ADCP and XCP-derived velocity profiles. Combined ADCP, GPS, and XCP random errors yield a standard error in individual water velocity profiles that varies with GPS quality and ship motion but is approximately  $0.02 \text{ m s}^{-1}$  for most of the measurements discussed here (and up to  $0.05 \text{ m s}^{-1}$  at times). Much of this error is in the depth-independent correction by GPS and ADCP, while the XCP relative velocity profile is generally accurate to better than  $0.01 \text{ m s}^{-1}$ .

#### b. Estimating bottom stress

Bottom stress is an important parameter affecting the path and speed of a bottom-intensified flow such as the DSO. In the absence of a density stratification or buoy-



TABLE 1. Statistics of measured bottom-layer properties from all XCP/XCTD/CTD profiles used in section analyses and containing dense ( $\sigma_\theta > 27.8$ ) water:  $h_{\text{MLT}}$  and  $h_{\text{MLD}}$  are mixed layer thickness determined by temperature and density changes of  $0.02^\circ\text{C}$  and  $0.03 \text{ kg m}^{-3}$  respectively,  $h_{27.8}$  and  $u_{27.8}$  are the thickness and mean velocity of the overflow layer (defined by  $\sigma_\theta > 27.8 \text{ kg m}^{-3}$ ), and  $N_{\text{ML}}$  is the buoyancy frequency estimated by a robust linear fit of density to a height  $h_{\text{MLD}}$  above the bottom.

Quantity	(Units)	No.	Min	25%ile	Median	75%ile	Max	Mean
$h_{\text{MLT}}$	(m)	67	2	24	40	65	217	53
$h_{\text{MLD}}$	(m)	67	8	34	56	94	334	77
$h_{27.8}$	(m)	67	15	94	150	213	491	157
$ u_* /N_{\text{ML}}$	(m)	57	1	15	46	$\infty$	$\infty$	33*
$ u_{27.8} $	(m s $^{-1}$ )	64	0.09	0.29	0.49	0.78	1.32	0.56
$ u_* $	(m s $^{-1}$ )	62	0.002	0.017	0.026	0.037	0.074	0.029
$(u_* \cdot u_{27.8})$	(m s $^{-1}$ )	60	-0.0004	0.016	0.022	0.036	0.070	0.027
$ u_* \times u_{27.8} $	(m s $^{-1}$ )	60	-0.034	-0.0073	-0.0018	0.0035	0.037	-0.0017
$ u_{27.8} $	(m s $^{-1}$ )	62	$2 \times 10^{-5}$	0.001	0.010	0.052	8.5	0.24
$N_{\text{ML}}$	(s $^{-1}$ )	66	0	0	0.0006	0.0013	0.0033	0.0008

\* Mean of 38 noninfinite values.

ancy flux through the boundary, the near-bottom velocity often follows the “law of the wall”:

$$u(z) = \frac{u_*}{\kappa} \ln\left(\frac{z}{z_0}\right). \quad (1)$$

Here,  $u_*$  is the friction velocity, a measure of the magnitude of turbulent fluctuations;  $\kappa = 0.4$  is the von Kármán constant; and  $z_0$  is the roughness length. The slope of a linear fit to the observed  $u$  versus  $\ln z$  (Fig. 3) is  $u_*/\kappa$ , giving an estimate of boundary shear stress,  $\tau = \rho u_*^2$ .

Statistics of these quantities are shown in Table 1. Errors in reference velocity do not affect this estimate of  $u_*$ , although they do affect  $z_0$ , the  $z$ -axis intercept. For this reason, we are less confident about the  $z_0$  estimates. The direction of the stress is determined by rotating the velocity components until all of the stress is in one component. Because of the velocity rotation in the planetary boundary layer, this direction is normally to the left of the overlying velocity, as indicated by the negative median and mean of  $|u_* \times u_{27.8}|$  in Table 1.

While theoretical and laboratory studies have derived the logarithmic velocity shape for time-averaged velocity profiles, rather than instantaneous ones, this fitting technique has been successfully applied to XCP data a number of times, including in the Mediterranean outflow (Johnson et al. 1994a,b) and the Faroe Bank Channel (Johnson and Sanford 1992). The reason for its success is attributed to the fact that, in general, deviations from the logarithmic shape should only be on the order of the magnitude of  $u_*$ , which is usually substantially smaller than the velocity range in the boundary layer. Figure 3 supports this conclusion.

The correct boundary layer height over which to fit remains the subject of some debate. For example, Sanford and Lien (1999) have found systematic differences between stresses estimated from logarithmic fits over

the layer 0–3 m versus the layer 5–12 m. They suggest that the former is the “true” layer of boundary (or wall) turbulence while the latter is dominated by form drag and represents the actual stress exerted by the bottom on the flow. If this is correct, our choice of the bottom 16 m should give a meaningful value for the momentum balance of the overflow, and is thick enough so that the XCP yields a suitable number of points to fit.

### c. Streamtube framework

In its most basic description, the DSO can be thought of as a slab of dense water under the influences of gravity, friction, and Coriolis acceleration sliding down the continental slope through a stratified background (Fig. 4). The flow trades the potential energy it possesses through its density anomaly and height on the slope for downstream kinetic energy, which is in turn 1) used to accelerate ambient fluid entrained into the flow and 2) extracted by turbulent stresses in the bottom boundary layer.

This essentially one-dimensional “streamtube” approach was taken by Smith (1975) and Killworth (1977) in describing the DSO and Weddell Sea deep-water formation. Price and Baringer (1994) extended the streamtube description through improved friction and a Richardson number-dependent entrainment scheme and applied it to a number of both high- and low-latitude outflows. Of all of these, the DSO is possibly the most problematic because of its highly variable nature and full-water-column flow.

In the streamtube framework, cross-isobath transport and release of available potential energy (APE) are firmly linked to the overflow’s ability to overcome the constraints of geostrophic balance, which tends to prevent APE release. One way for geophysical fluids to release APE is through friction, which reduces velocities and resulting Coriolis accelerations. The inset force triangle

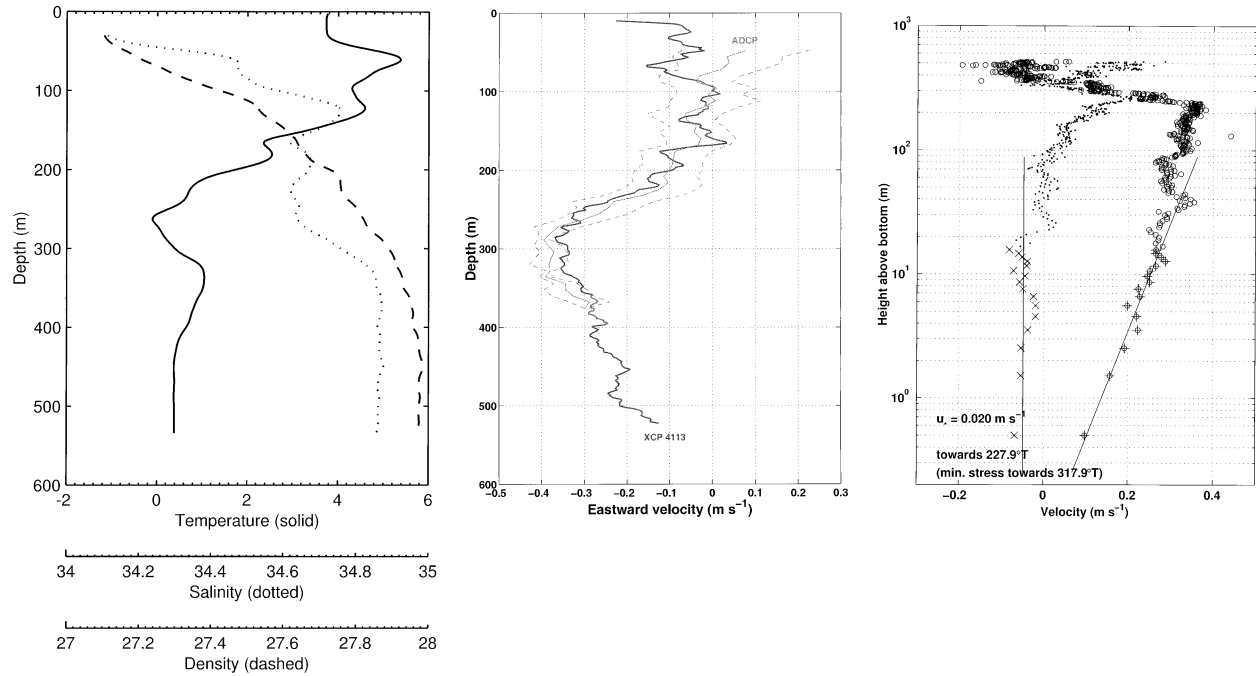


FIG. 3. A sample profile showing (left) near-sill  $T$ ,  $S$ , and  $\sigma_\theta$  structure, (middle) the match of XCP and ADCP velocities, and (right) the logarithmic velocity fit to the bottom 15 m of the XCP. Both panels are from the same XCP drop (4113), but the middle panel shows the (geographic) eastward component only while the right shows the components in the directions of maximum (Os) and minimum (dots) log-layer stress. Data points used in the log fit are indicated by large crosses and Xs, respectively.

in Fig. 4 illustrates how the resulting balance between downslope gravitational force, Coriolis force, and retarding friction produces an angled path, with the flow's downward angle decreasing as slope and density anomaly decrease through entrainment or flow into denser background water or less-steep topography. This force balance allows the calculation of the rate of change in water depth ( $H_b$ ) along the overflow's path ( $\xi$ ) as simply

$$\frac{dH_b}{d\xi} = \sin\alpha \sin\beta = \frac{\tau}{\rho'gh}, \quad (2)$$

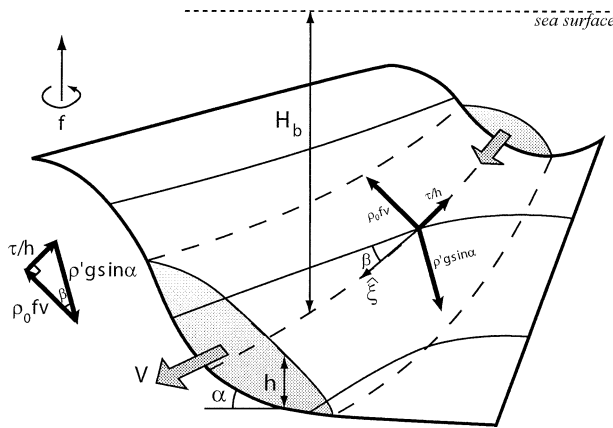


FIG. 4. Schematic illustration of the streamtube concept and definition of symbols used in the text. The three main forces on the overflow (buoyancy, drag, and Coriolis) are indicated by arrows, with the resulting triangle forming the basis for Eq. (2).

where  $\rho'$  and  $h$  are the density anomaly and thickness of the overflow layer and  $\tau$  is the component of the combined bottom and interfacial stress opposing the layer's velocity. We will use Eq. (2) to test the hypothesis that the descending pathway and accompanying APE release of the DSO can be explained by frictional stresses in the bottom and interfacial boundary layers. While it is clear that the DSO is not a "steady" flow in an instantaneous sense, we will use spatial and temporal averaging to evaluate the dynamical balances of the statistically steady (over intervals of a week or longer) flow.

#### d. Computation of integral properties from observed sections

In order to investigate a streamtube description of overflow dynamics from real observations and sampling patterns, it is necessary to make some compromises. The true structure of flow and hydrography involves far more complex patterns than the simple one-dimensional properties of the streamtube, so choices in how to average or transform the observations into the desired integral quantities for comparison may have an impact on the credibility of the model.

First of all, we have chosen to define the overflow in terms of density, including all water with  $\sigma_\theta > 27.8$  kg

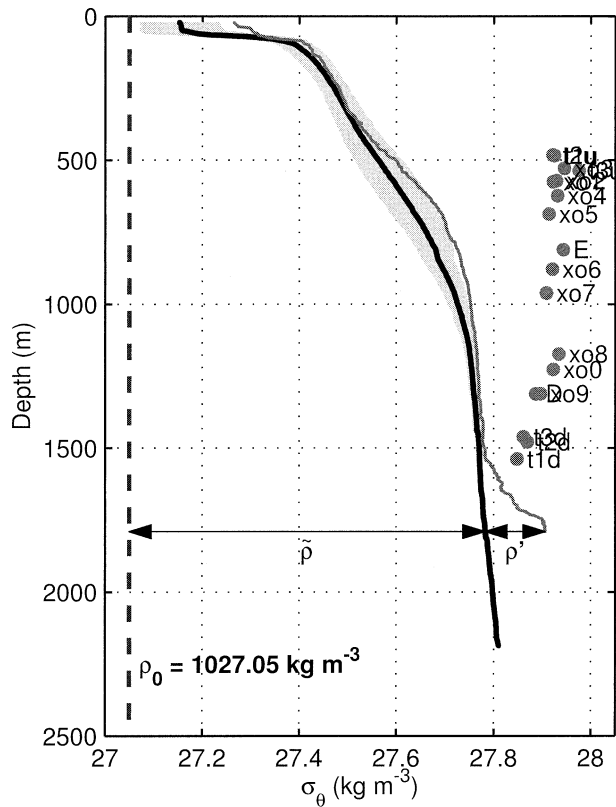


FIG. 5. Decomposition of density into constant, stratified background and anomaly contributions. The thin line is a typical overflow density profile (from section t3d). The thick line is the mean background ( $\bar{\rho}$ ) density profile from several profiles in deep water either above or beyond the boundaries of the overflow water, with gray shading covering the 1 standard deviation envelope. Also shown (dots) are the overflow mean bottom depth ( $\bar{H}_b$ ) and density ( $\bar{\sigma}_\theta$ ) for each of the sections discussed here, as presented separately in Figs. 7 and 10.

$\text{m}^{-3}$ , following Dickson and Brown (1994).<sup>1</sup> The two most likely problems with a fixed-density definition of the overflow are 1) a background density approaching the defining isopycnal, leading to an overestimate of transport, or 2) the mixing of overflow water with background water to produce anomalous fluid falling outside of the overflow definition, leading to an underestimate of transport. Fortunately, the  $\bar{\rho}$  profile constructed from stations in the interior of the Irminger Basin does not reach  $27.8 \text{ kg m}^{-3}$  until 2000-m depth (essentially the maximum depth reached by the overflow in the survey area). As evident from Fig. 5, the amount of water between the background density and  $27.8 \text{ kg m}^{-3}$  is fairly small as long as the bulk of the overflow is sufficiently denser than  $27.8 \text{ kg m}^{-3}$ . As more mixing occurs, the

<sup>1</sup> In the discussions that follow, density ( $\rho$ ) will always refer to potential density referenced to the surface and  $\sigma_\theta = \rho - 1000$ . At times it will be convenient to decompose density into a constant mean ( $\rho_0$ ), stratified background ( $\bar{\rho}$ ), and anomaly ( $\rho'$ ) so that  $\rho = \rho_0 + \bar{\rho}(z) + \rho'(x, \xi, z, t)$  (Fig. 5).

underestimate of transport due to this intermediate layer could become important. Although both of these effects have the potential to lead to transport errors farther downstream where the overflow is less well defined, in the region described here neither appears to contribute significant errors.

The sections making up our survey were not always straight lines and were not always perpendicular to the overflow's path. In order to estimate along-section distance, then, the station positions have all been projected onto a best-fit line for the section. When cross-sectional area is important, the approximate angle,  $\theta$ , of this line to the flow path normal has been estimated and used as a scaling factor for integrated values. For example, the cross-sectional area of the overflow is

$$A = \cos\theta \iint_A dz dx = \cos\theta \int_w h dx, \quad (3)$$

where  $h$  is then the thickness of the overflow layer and  $\iint_A$  specifies an integration over the cross-sectional area of the overflow water (i.e., between the  $27.8$  isopycnal and the bottom). In general, most such areal integrations are constructed by deriving averages for the overflow layer in each profile, along with thickness  $h$ , and then integrating across the width of the dense water ( $\int_w dx$ ) using the trapezoidal method. Figure 6 shows an example of the cross-stream profiles of  $h$ ,  $\rho'$ ,  $v$ , and  $\tau_b$  from survey section t1d. Note that the cross-stream coordinate  $x$  [labeled "Distance (km)" in Fig. 6] in Eqs. (3)–(9) is defined independently for each section, generally relative to the station farthest upslope.

The scaling factor  $\theta$  is not used when through-section property fluxes are calculated, since the integrated velocity perpendicular to the section is independent of angle. For example, the volume transport of overflow water is

$$Q = \iint_A v dz dx = \int_w \bar{v} h dx, \quad (4)$$

where  $v$  is the component of velocity perpendicular to the best-fit section line and  $\bar{v}$  is the layer mean for a single profile.

Certain mean quantities for streamtube comparison can be equivalently derived from others, such as an overall velocity

$$V = \frac{\iint_A v dz dx}{A} = \frac{Q}{A}. \quad (5)$$

Many of the results presented in this paper deal with density-anomaly-weighted averages of various properties, which are compared to the constant properties assumed by the streamtube model. This approach has been employed using data from a survey of the Mediterranean outflow (Baringer and Price 1997) with considerable

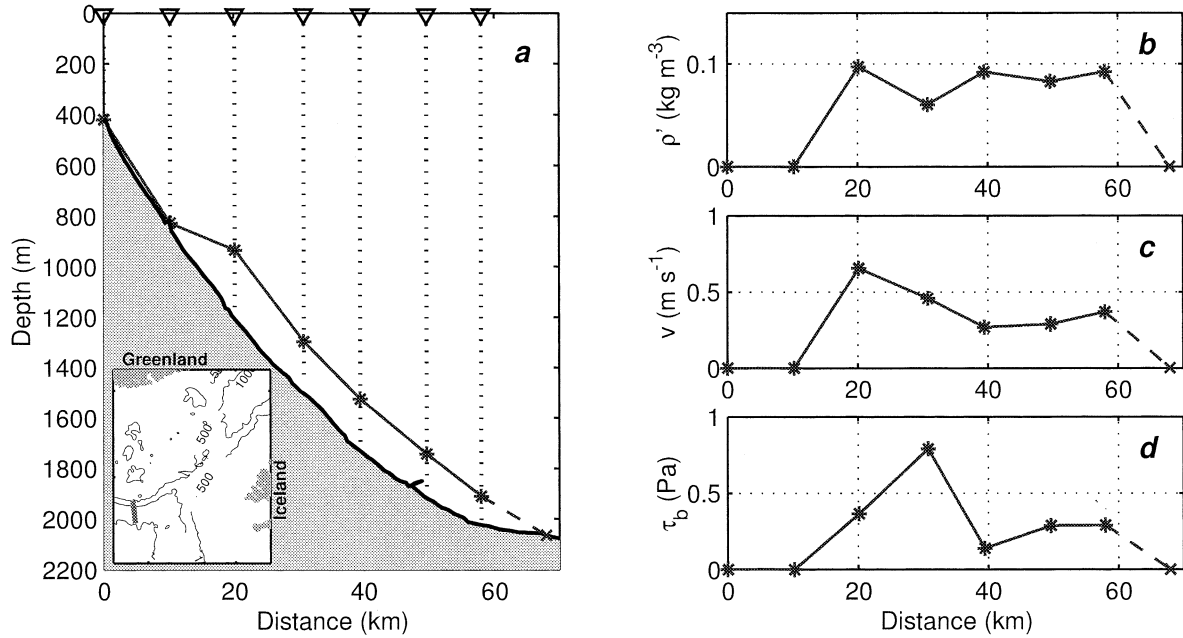


FIG. 6. Example of overflow properties from a typical cross-stream section (t1d): (a) the depth of the 27.8 isopycnal defining the overflow water (dotted lines indicate profile locations), (b) mean overflow density anomaly  $\rho'$ , (c) mean overflow velocity  $v$ , and (d) component of bottom stress  $\tau_b$ , perpendicular to the section. Dashed lines at the end of each section indicate the extrapolation to zero overflow water over 10 km if still present.

success. Two of the simplest such quantities to define are the position of the center of mass anomaly

$$X = \frac{\iint_A \rho' x \, dz \, dx}{\iint_A \rho' \, dz \, dx}, \quad (6)$$

and the anomaly-weighted bottom depth,

$$\overline{H_b} = \frac{\iint_A \rho' H_b \, dz \, dx}{\iint_A \rho' \, dz \, dx} \quad (7)$$

(note that both  $x$  and  $H_b$  are independent of  $z$ ).

Some uncertainty arises when the stations did not span both edges of the overflow water. In these cases, we have applied an extrapolation of overflow water to zero thickness at a distance 10 km beyond the end of each section (see Fig. 6) but have also generated “error bars” whose lower limit derives from cutting off the integration at the last station and whose upper limit results from a constant-value extrapolation to 10 km. Large error bars, then, are an attempt to convey the lack of certain knowledge of overflow extent, although in most cases the 10-km extrapolation to zero does seem to be a reasonable guess, with the error bars generally producing (in our opinion) overestimates of the probable error.

The calculation of mean quantities presents special problems for those values that could tend to disproportionately weight the overflow edges, such as a mean thickness. Even more difficult is an estimate of overflow width, since many sections did not reach the limit of the overflow water at both ends, while most sections did cover the vast majority of overflow volume. One way around this is through the use of a plume “half width,”  $W_{0.5}$ , defined such that the middle 50% of the mass anomaly is contained within a width  $W_{0.5}$ . A reasonable estimate of the mean thickness is then given by  $H = A/(2 \times W_{0.5})$ .

## 4. Results

### a. Pathway and descent

The geographical distribution of  $X$  from all 18 sections is shown in Fig. 8 (dots), along with estimates of  $W_{0.5}$  (bars). Despite the great deal of temporal variability in overflow transport, thickness, and velocity the mean path appears quite stable. Cross-stream variability in  $X$  decreases from only 15 km or so within the first 50 km of the sill to less than 5 km at the western edge of the domain, just over 220 km from the sill.

As shown in Fig. 7, the plume descends relatively slowly at first (during the first 50 km from the sill) and then at a more-or-less constant rate of 6 m km<sup>-1</sup>. This descent is substantially more rapid than the 2.5 m km<sup>-1</sup> (or 1/400 slope) predicted by Killworth (2001), using a

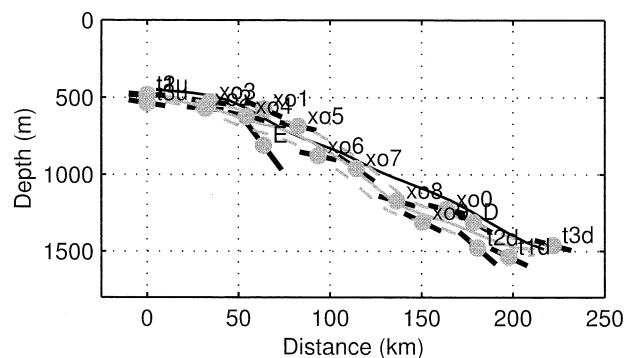


FIG. 7. The descent of the overflow with distance ( $\xi$ ) from the sill (including sections E and D from the *Aranda* cruise). The dots show  $H_b$ , the mass-anomaly-weighted bottom depth of the plume [Eq. (7)] for each section. The short thick angled lines indicate the rate of descent,  $dH_b/d\xi$ , expected from a simple balance between buoyancy, Coriolis force and friction, including contributions from both bottom stress and entrainment [Eq. (2)]. The thin gray and black lines compare the 20-km Gaussian window smoothed  $H_b$  values and smoothed integration of  $dH_b/d\xi$ , respectively. Dashed gray lines indicate the estimated standard error in the smoothed  $H_b$  curve. Extrapolation error bars for each section are smaller than the plot symbols.

local equilibrium solution for a turbulent boundary layer (Zilitinkevich and Mironov 1996).

The angled bars in Fig. 7 show the slope in plume depth versus distance expected from Eq. (2), using mean quantities determined at each section.

While the bottom stresses, and, hence, the expected rates of descent, do vary considerably from section to section, the plume depth shown in Fig. 7 is the result of the integrated history of descent that the flow has undergone since the sill, and so is expected to be substantially smoother than other in situ properties. This might not be the case, however, if the inhomogeneities in  $\tau$  were linked to individual water parcels (say, propagating boluses or pulses that carry anomalous water and isolate it from its surroundings). The relative variance in  $\tau$  and depth, then, holds important implications for the phenomenology of the overflow pulses and sets a limit on the internal isolation of features.

#### 1) DRAG COEFFICIENT

The log-fit determined values of bottom stress can be compared to the absolute speed of the water to estimate a drag coefficient. In aggregate (Fig. 9), bottom stress estimates yield  $C_D = (2.9 \pm 0.4) \times 10^{-3}$ , in good agreement with other studies of oceanographic flows. The uncertainty estimate is an attempt to summarize a variety

### Overflow Path

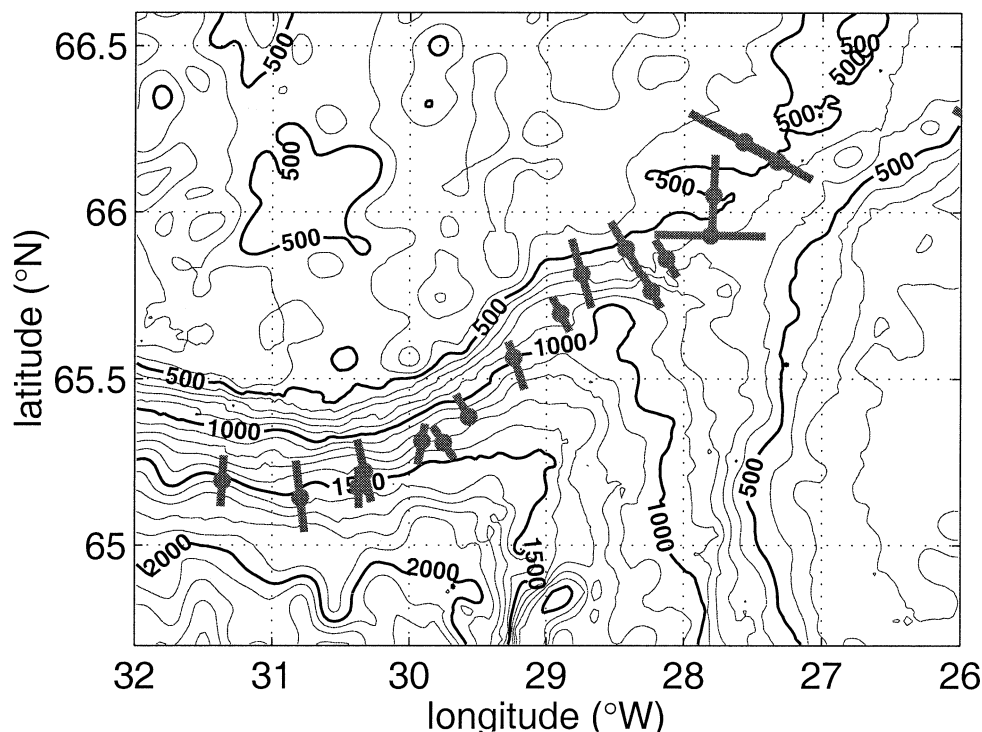


FIG. 8. Position of overflow center of mass ( $X$ ) and half-width ( $W_{0.5}$ ) on each of 18 cross sections. Apart from some variability at the sill and early in the descent, the flow follows a well-defined path with remarkably little cross-stream scatter.



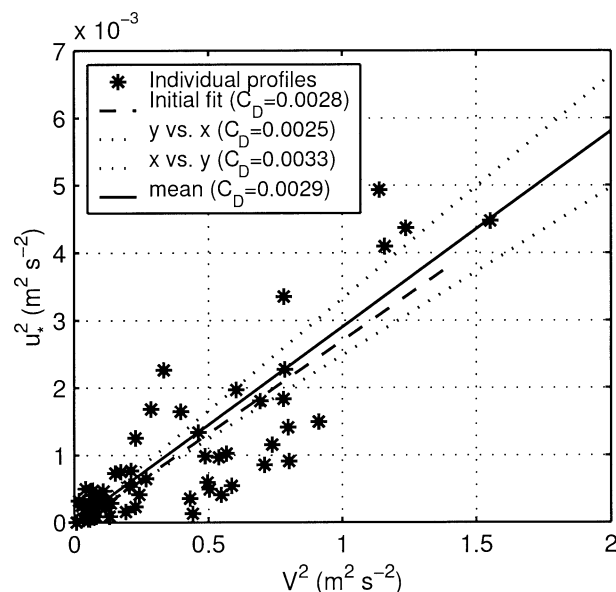


FIG. 9. Best guesses at  $C_D$  from linear fit of  $u_*^2$  vs  $V^2$ , using the 60 profiles from 1997 and 1998 with dense bottom water;  $u_*$  is the component of friction velocity parallel to the dense layer velocity and  $V$  is the layer speed. The dashed “initial fit” line is a standard linear least squares fit, while the two dotted lines are robust linear fits based on minimizing the summed absolute deviation in  $u_*^2$  and  $V^2$ , respectively, as well as being forced to pass through the origin. The solid line is the mean of these two robust fits.

of measures of central tendency, including average ratios and slopes of fits as shown in Fig. 9. The variance among individual profiles is much larger.

Experiments with a high-resolution regional model (Käse and Oschlies 2000) as well as earlier results from simpler models (Smith 1975; Price and Baringer 1994; Jungclaus and Backhaus 1994), have shown that the pathway of the overflow plume depends strongly on the amount of bottom friction used. The model’s (linear) drag coefficient that appears to give the best agreement with the measured pathway, though, yields a substantially lower bottom stress value than the median obtained from our observations.

## 2) INTERFACIAL STRESS

The stress exerted on the plume at the interface through turbulent momentum transfer (or, equivalently, through the entrainment of slower water) may be an important term in the momentum balance. Assuming a steady and continuous flow, Johnson et al. (1994b) used XCP and hydrographic sections across the Mediterranean outflow plume to compute a bulk estimate of the vertical turbulent buoyancy flux, calculated from the residual of mass and volume fluxes, combined with assumptions about the relative magnitudes of buoyancy flux and dissipation.

## 3) OTHER MECHANISMS FOR CROSS-ISOBATH TRANSPORT

Unsteady patterns of flow produced, for example, by baroclinic instability could also permit violation of the steady geostrophic constraint, allowing APE release and descent across topography. However, the potential for linear instability of the DSO in the region of steep plume descent is limited by the magnitude of the slope there (Swaters 1991). A number of studies have examined the mechanism of baroclinic instability and its effectiveness in transporting dense water down slopes. In particular, Jungclaus et al. (2001) have pointed out the tendency to form cyclones in an initially steady alongslope flow with scales similar to the DSO, although full development takes longer than the 4 days or so needed for the flow to transit our survey region. Hydrographic measurements from the *Poseidon* suggest that eddy-induced spreading may be more important beyond 200 km from the sill, allowing for ongoing instability as a probable cause in that region (Käse et al. 2003). It may also be possible that flow instability is initiated earlier, over the gradual topography of the sill region. In this case, the inhomogeneities produced near or before the sill could become amplified during the descent of the slope. In this case, the models of Smith (1976) or Fristedt et al. (1999) would be more applicable.

### b. Mixing and momentum

In addition to the loss of potential energy due to its descent, the plume’s density anomaly also undergoes substantial dilution with distance from the sill. This dilution is clearly due to mixing with the surrounding waters, but the relative importance of vertical processes (such as Kelvin–Helmholtz instability at the interface) and horizontal stirring by eddies is not yet entirely certain. In either case, the addition of nonmoving ambient fluid acts to reduce the kinetic energy of the flow while conserving momentum. This slowing is termed “entrainment stress.”

In most cases throughout our survey region, the  $\sigma_\theta = 27.8$  bounding isopycnal intersects the bottom at both edges of the plume, requiring any density changes below this boundary to be due to diapycnal processes. As long as this boundary remains close to the boundary of the “anomalous” fluid ( $\rho' = 0$ ; see Fig. 5), we can use a single quantity with units of velocity to describe both the net mass flux across the plume boundary and the diffusive influx of background properties. This “entrainment velocity” ( $w_e$ ) has been used diagnostically by many authors, despite a great deal of uncertainty about the exact process it represents (Turner 1986; Oakley and Elliott 1980; Price and Baringer 1994).

The interpretation of  $w_e$  becomes more problematic if there is substantial mixing between the boundary fluid itself and the background, producing anomalous fluid “outside” the defined plume. In such a situation, a dis-

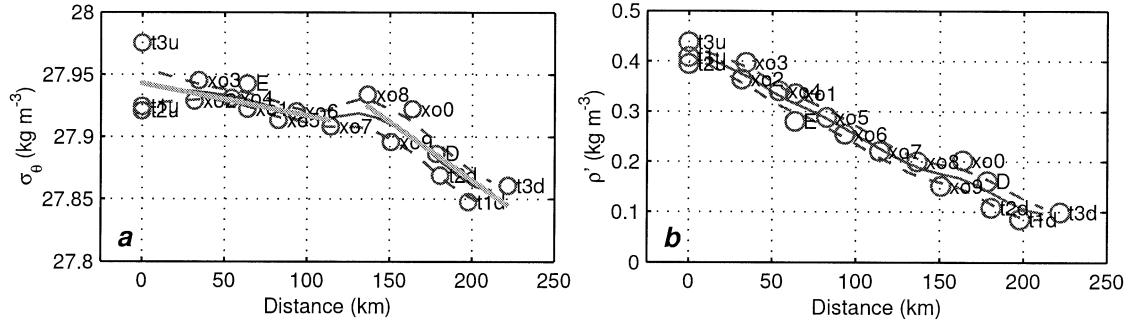


FIG. 10. Evolution of plume density ( $\bar{\sigma}_\theta$ ) and density anomaly ( $\bar{\rho}'$ ) with distance from the sill. Solid and dashed curves show the sliding mean and standard error with a 20-km Gaussian window. The two thick straight lines in (a) are from linear fits to the regions before and after 125 km, and appear to show a significant change in slope. Extrapolation error bars for each section are smaller than the plot symbols.

inction could be made between the dilution caused by diffusive mixing across the boundary and that caused by a net inflow of mass. In our data, the amount of anomalous fluid outside the  $\sigma_\theta = 27.8$  boundary is generally small, so we have chosen to ignore this distinction. A finer density resolution and better sampling statistics would allow this to be investigated further.

#### 1) PROPERTY CHANGES

Both average density,

$$\bar{\sigma}_\theta = \frac{\iint_A (\rho - 1000) dz dx}{\iint_A dz dx}, \quad (8)$$

and density anomaly from the background,

$$\bar{\rho}' = \frac{\iint_A (\rho - \rho_0 - \bar{\rho}) dz dx}{\iint_A dz dx}, \quad (9)$$

decrease with distance from the sill (Fig. 10), with the  $\bar{\rho}'$  decrease being, of course, larger due to the increasing background density as the plume descends.

The decrease in  $\bar{\sigma}_\theta$ , however, can only be due to the entrainment of ambient fluid and appears to become steeper beyond  $\sim 125$  km from the sill. If the slopes in Fig. 10 do represent a statistically steady state, then entrainment can be estimated from the rate of  $\bar{\sigma}_\theta$  decrease with distance. Following the streamtube with downstream velocity  $V$ , the local rate of change depends on the entrainment rate ( $w_e$ , with units of velocity) as well as the layer thickness  $H$  and the density anomaly being entrained ( $-\bar{\rho}'$ ):

$$\frac{d\bar{\sigma}_\theta}{dt} = -V \frac{\partial \bar{\sigma}_\theta}{\partial \xi} = -\frac{\bar{\rho}' w_e}{H}, \quad (10)$$

where  $\xi$  indicates the downstream coordinate, as shown in Fig. 4 [see also Eq. (4) in Price and Baringer (1994)]. The entrainment rate can then be determined from measured quantities:

$$w_e = \frac{VH}{\bar{\rho}'} \frac{d\bar{\sigma}_\theta}{d\xi}. \quad (11)$$

Using the slopes shown in Fig. 10 to estimate  $d\bar{\sigma}_\theta/d\xi$  for the two regions before and after 125 km from the sill, combined with mean values of  $V$ ,  $H$ , and  $\bar{\rho}'$  in each region, indicates more than an order of magnitude increase in  $w_e$  from  $6 \times 10^{-5}$  to  $8 \times 10^{-4}$  m s $^{-1}$ .

The above analysis can be done with any conservative tracer to yield independent estimates of entrainment velocity (with an accuracy that depends on the magnitude and robustness of the anomaly and rate of change with distance). Since our profilers measured overflow temperature and salinity separately, we have examined both for confirmation of the above result. Temperature is the major factor controlling the density contrast between the overflow and background, so the changes in temperature and temperature anomaly with distance are similar in character to changes in density and density anomaly. The  $w_e$  values estimated from temperature changes are  $4 \times 10^{-5}$  and  $8 \times 10^{-4}$  m s $^{-1}$  (before and after 125 km, respectively), very close to those determined from density. Salinity, on the other hand, is not as easy to use for this sort of analysis since it does not vary monotonically with depth and is dominated by the intermittent presence of fresh Polar Intermediate Water (PIW) located at or immediately above the plume interface. In fact, while the overflow layer is on the whole fresher than the background water, the mean salinity actually decreases slightly in the region up to 125 km from the sill, possibly due to the initial entrainment of PIW. After 125 km the salinity does increase, but the slope is not very significant.

The increase in  $w_e$  diagnosed from density and temperature changes could be the result of a decrease in bulk Richardson number,

$$Ri_b = \frac{\overline{\rho'} g H}{\rho_0 V^2},$$

as the plume anomaly decreases (average  $\overline{\rho'}$  goes from 0.34 to 0.14 kg m<sup>-3</sup>) and thickness increases (average  $H$  goes from 150 to 240 m). However, the large variability in thickness and velocity make the significance of this decrease difficult to determine. Estimates from section-averaged quantities do show a larger fraction of  $Ri_b < 1$  values beyond 125 km from the sill and the mean  $Ri_b$  over the regions before and after 125 km are 1.8 and 1.2, respectively.

Another possibility is that it is a change in background stratification itself that is responsible for this increase in entrainment. The background stratification ( $\partial\bar{\rho}/\partial z$ ) does decrease from  $4 \times 10^{-4}$  to  $6 \times 10^{-5}$  kg m<sup>-4</sup> ( $N$  drops from  $2 \times 10^{-3}$  to  $8 \times 10^{-4}$  s<sup>-1</sup>) fairly abruptly at around 1000 m, which is also the depth reached by the overflow at the point of  $w_e$  increase (see Fig. 7). While the large stratification at the layer interface has been the focus of most investigations, the weaker stratification above the interface might have an influence on the shape and penetration of the eddies that drive the entrainment.

From the few existing microstructure measurements at the overflow interface, Oakey and Elliott (1980) concluded that “vertical diffusion is not an important heat source to the overflow in this region.” However, it is not clear whether these measurements (taken at a single location on the O73 current meter line—approximately 50 km from the sill and in water depth approximately 500 m) adequately sampled the processes, such as Kelvin–Helmholtz billows, which would affect the bulk of the overflow. They certainly did not cover the region of high entrainment diagnosed from this study. Nevertheless, the specific process responsible for the inferred  $w_e$  remains unidentified.

In addition to its consequences for overflow mean density,  $w_e$  should have a profound effect on transport changes resulting from the inclusion of new water. Figure 11 shows the through-section transport ( $Q$ ) of  $\sigma_\theta > 27.8$  kg m<sup>-3</sup> water on all sections, demonstrating that the effect of entrainment may be particularly difficult to pick out of the short-term variability present in the measurements. Although the integrating effect mentioned above in section 4a should apply to total transport as well, the constituent measurements of velocity ( $V$ ) and cross-sectional area ( $A$ ) are themselves highly variable (see Fig. 12). In fact, a substantial fraction of total transport may be due to the covariability of these quantities, casting further doubt on the simplified streamtube model.

Immediately, complications come to mind due to the fact that the overflow does not, in fact, have only a single velocity and density and the overlying water is neither motionless nor uniform in structure from station to station. However, it is important to know how close the reality comes to following these idealized models

and whether the dominant force balances are as they describe.

## 2) ENTRAINMENT STRESS

Using the estimates of  $w_e$  above, it is possible to estimate the effective mean entrainment stress as  $\tau_i = \rho_0 V w_e$ , where  $V$  is the overflow layer velocity (Price and Baringer 1994). Taking 0.6 m s<sup>-1</sup> as a reasonable mean velocity over the entire region (from Fig. 12), the  $\tau_i$  values estimated in the low-entrainment and high-entrainment regions are 0.04 and 0.8 Pa, respectively. These can be compared with the overall mean section-averaged bottom stress ( $\tau_b$ ) of 1.7 Pa (where section averages range from 0.5 to 4 Pa on individual sections). If the high-entrainment region diagnosed from  $\sigma_\theta$  changes is, in fact, a real feature of the DSO, then it is clear that entrainment stress could play a significant role in the momentum balance of this region.

## 5. Discussion

We have claimed that the rate of descent of the DSO plume across topography is controlled by bottom-boundary shear stress operating on the plume as a whole, almost as a solid body. It is worthwhile to point out that the importance of such stress may be reduced in cases where the near-bottom stratification and topographic slope are substantial. As described by MacCready and Rhines (1993), cross-slope buoyancy transport by the bottom Ekman layer can lead to both a shutdown of the Ekman flow and a reduction in near-bottom velocities through thermal wind shear. This process has the potential to greatly reduce the energy lost to turbulent stresses.

Surprisingly enough, however, the plume-averaged force balance in the region of the DSO described here does not show evidence for a “slippery bottom boundary layer” of this sort. For one thing, the interior of the overflow is not noticeably stratified in the cross-stream direction, making any interior Ekman flow ineffective in producing buoyancy forces. This same difficulty was noted in a survey of the deep western boundary current at the Blake Outer Ridge (some 6000 km downstream of the Denmark Strait) (Stahr and Sanford 1999). This may point toward a substantial difference between the type of boundary layer beneath a plume of anomalous fluid entering (under its own power) a stratified ocean and the general case of a boundary layer beneath a stratified current (driven by external forces).

One of the goals of the intensive study in the entrainment region of the DSO is to elucidate the mechanism behind the dramatic increase of transport noted by Dickson and Brown (1994) from 2.9 Sv near the sill to 5.2 Sv at the Dohrn Bank array, 160 km downstream. As shown by Fig. 11, our measurements do yield the appropriate amount of entrainment to gain this increase, despite the fact that the transport measurements from

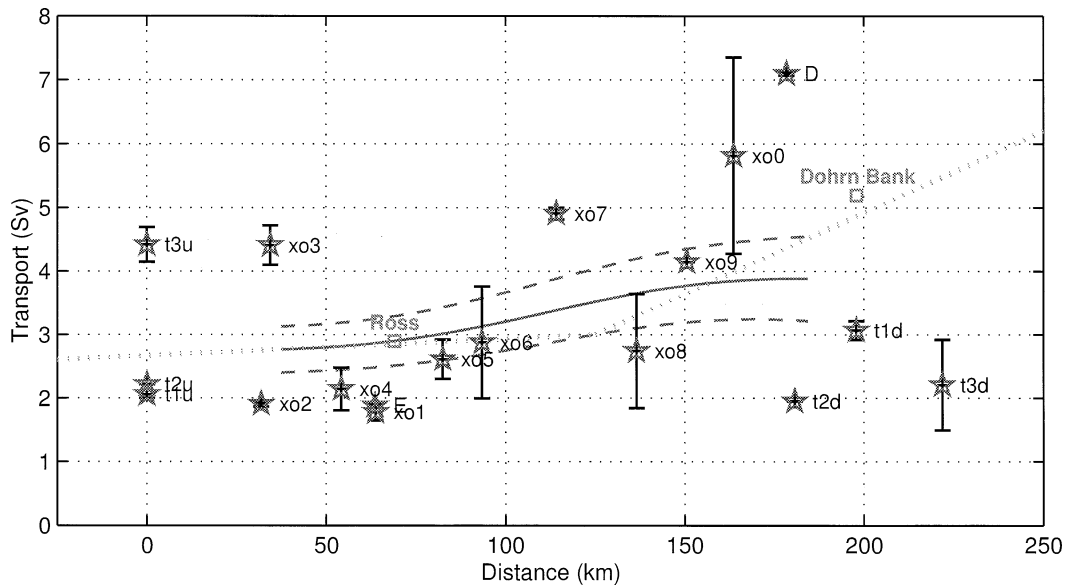


FIG. 11. Transport ( $Q$ ) of  $\sigma_\theta > 27.8$  water vs distance from the sill, as measured by all 18 sections with XCPs (including two from the *Aranda*) as well as two current meter arrays (labeled as “Ross” and “Dohrn Bank”) (Ross 1984; Dickson and Brown 1994). The dotted line with break in slope at 125 km shows the projected transport derived by starting with the Giron et al. (2001) value of 2.7 Sv at the sill and increasing because of entrainment at rates ( $w_e$ ) of  $6 \times 10^{-5} \text{ m s}^{-1}$  and then  $8 \times 10^{-4} \text{ m s}^{-1}$  [estimated from Eq. (11) and solid lines in Fig. 10] over widths of 44 and 32 km (average values of  $2W_{0.5}$  in the regions before and after 125 km, respectively). The solid and dashed curves indicate the sliding mean and standard error with a 75-km Gaussian window. Error bars represent the estimated uncertainty due to extrapolation when not all dense water was covered by the section (see section 3d). In some cases, error bars are smaller than the plot symbols.

the survey are heavily aliased by temporal variability. We emphasize again that the *density* measurements (Fig. 10) do not appear to be substantively affected by the same processes that produce this aliasing and that the estimated entrainment rates from plume dilution are consequently more robust than any conclusions made from the transport values alone.

The possibility of an alternate pathway for some of the flow that misses the O73 current meters but rejoins before the Dohrn Bank array has been suggested by some hydrographic surveys (Rudels et al. 1999). However, this option is not necessary unless the overflow entrainment is significantly weaker than suggested by

our bulk estimates of  $w_e$  based on the dilution of the plume with distance from the sill. In addition, the pathway of the majority of the overflow water, shown in Fig. 8, exhibits strikingly little meandering behavior despite the large temporal variations in transport. This steady pathway does not leave much room for extra branches high on the shelf.

A question that has not been answered by our study is the relative importance of vertical and horizontal processes in the dilution of the plume. A strong candidate for the entrainment mechanism is the more-or-less straightforward process of turbulent overturns driven by shear instability, possibly combined with stationary hy-

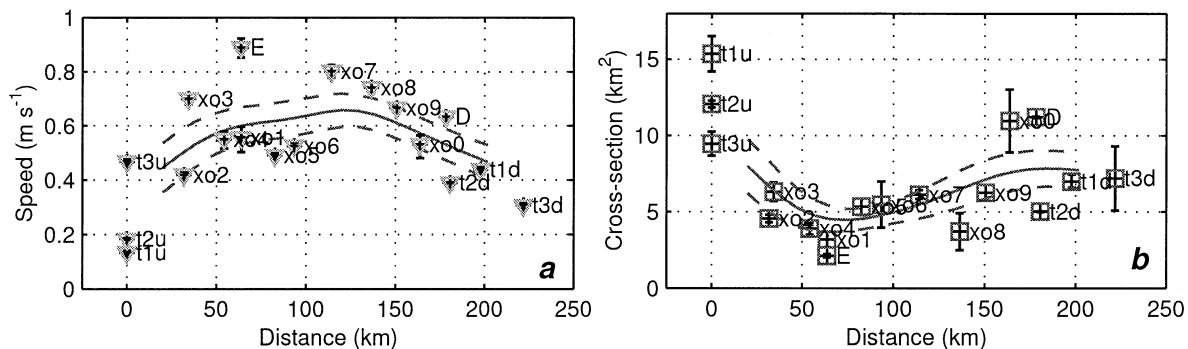


FIG. 12. Variation of plume velocity ( $V$ ) and cross-sectional area ( $A$ ) over distance from the sill. See Eqs. (5) and (3) for definitions of these section-averaged quantities. Solid and dashed curves indicate the sliding mean and standard error with a 40-km Gaussian window.



draulic jumps at locations of steep ridges or canyons in the topography. However, it is also quite possible that the flow variability in the form of eddies and downslope subplumes (Jiang and Garwood 1996) contributes substantially to the mixing of the fluid with the surrounding water. Although our definition of the overflow using an isopycnal surface implies that some sort of diapycnal process is required to produce entrainment, stirring by eddies could play a large role in enhancing this process through additional stretching and folding of material surfaces.

## 6. Conclusions

Girton et al. (2001) showed that there has been little change in either the magnitude of transport or the pattern of variability of the overflow between surveys in 1973 and 1998. Once this agreement over a 25-yr period is established, it becomes more plausible that significant features observed in the recent surveys can be considered universal characteristics of the DSO. In particular, the evolution of streamtube-averaged properties is important for diagnosing the forcing and modification the overflow undergoes in its path to becoming North Atlantic Deep Water.

In aggregate, the set of velocity and hydrography sections collected on the *Poseidon* and *Aranda* cruises, considered in the context of a streamtube description, capture a “zeroth order” picture of certain properties and dominant balances of the overflow. In particular, the pathway and descent of the plume are quite well defined over the first 250 km from the sill, apparently controlled by both the shape of the topography and the magnitude of bottom and interfacial stresses. At the same time, other properties, such as velocity ( $V$ ), cross-sectional area ( $A$ ), and transport ( $Q$ ) have much higher levels of variability, and are not quite so readily interpreted. Some aspects of this variability, as represented both in our observations and in a numerical model, are discussed by Käse et al. (2003).

The mean plume density (Fig. 10a) steadily decreases throughout the descent, with an apparent break in slope at 125 km indicating an increase in entrainment ( $w_e$ ) from  $6 \times 10^{-5}$  to  $8 \times 10^{-4} \text{ m s}^{-1}$  in the latter half of the survey area. This increase could be due to the larger topographic slopes in this region (see Fig. 13), in combination with the loss of density anomaly as the plume enters deeper water. Average Richardson numbers in these two regions do indicate less stability (and, hence, the likelihood of greater entrainment) in the latter region, but the difference is small. Curiously, the plume also encounters an abrupt reduction in background stratification ( $\sim 1000\text{-m}$  depth: see Fig. 5) and the plume-averaged mean velocity (Fig. 12) reaches a maximum at 125 km from the sill. It is not clear whether all of these events are related or, if so, which causes which.

The representation of density-driven overflows in the deep ocean continues to be a weak point in large-scale

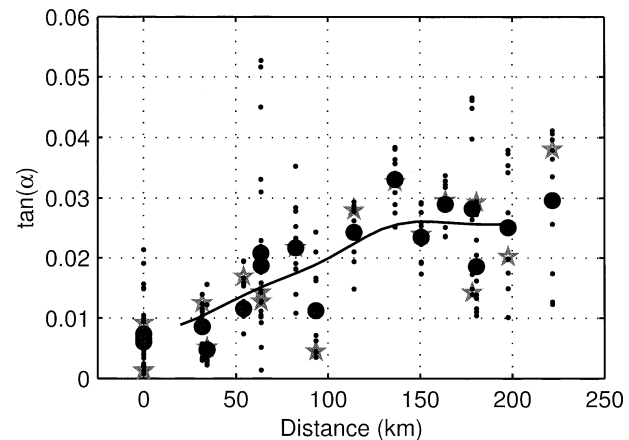


FIG. 13. Topographic slopes at each section computed by interpolation into the Smith and Sandwell (1997) bathymetry database. Large dots show the average slope over the width of each section. Stars indicate the slope under the center of overflow mass anomaly. Small dots show the slope at each station, indicating the range of slopes over each section. The solid curve is a smoothing of the average slopes using a 40-km Gaussian window.

numerical models. Nevertheless, the processes influencing rates of descent and entrainment are critically important to predicting the ventilation of those deep and bottom waters which are in turn a dominant part of the ocean's response to longer-term climate forcing. While the simple balance of Eq. (2) suggests some hope for bottom-boundary-layer models (e.g., Killworth and Edwards 1999), the descent that we compute using a constant quadratic drag coefficient of  $3 \times 10^{-3}$  to predict  $\tau$  is actually about 25% less than observed or computed using  $\tau$  measurements, hinting that such a simple drag law may not be adequate for ocean overflows. Of possibly even more importance is the need for an improved understanding of the entrainment process. Our observations present a target for future modeling studies, suggesting potential roles for both the background stratification (rather than simply the interface stratification alone) and topographic slope. It remains to be seen whether other overflow regions will exhibit similar dynamical behavior when subjected to equivalent observational scrutiny.

**Acknowledgments.** This work was supported by Grants OCE-9712313 and OCE-0099275 from the National Science Foundation. Ship time was provided by the German SFB-460 program and EC VEINS. Our collaborator, Rolf Käse, has provided invaluable assistance throughout all stages of the study.

## REFERENCES

- Aagaard, K., and S.-A. Malmberg, 1978: Low-frequency characteristics of the Denmark Strait overflow. ICES CM 1978/C:47, International Council for the Exploration of the Sea, Copenhagen, Denmark, 22 pp.
- Baringer, M. O., and J. F. Price, 1997: Momentum and energy balance

- of the Mediterranean outflow. *J. Phys. Oceanogr.*, **27**, 1678–1692.
- Dickson, R. R., and J. Brown, 1994: The production of North Atlantic Deep Water: Sources, rates, and pathways. *J. Geophys. Res.*, **99**, 12 319–12 341.
- , J. Lazier, J. Meincke, P. Rhines, and J. Swift, 1996: Long-term coordinated changes in the convective activity of the North Atlantic. *Progress in Oceanography*, Vol. 38, Pergamon, 241–295.
- Fristedt, T., R. Hietala, and P. Lundberg, 1999: Stability properties of a barotropic surface-water jet observed in the Denmark Strait. *Tellus*, **51A**, 979–989.
- Girton, J. B., 2001: Dynamics of transport and variability in the Denmark Strait overflow. Ph.D. thesis, University of Washington, Seattle, WA, 305 pp.
- , and T. B. Sanford, 1999: Velocity profile measurements of the Denmark Strait overflow. *International WOCE Newslett.*, No. 37, WOCE International Project Office, Southampton, United Kingdom, 28–30.
- , —, and R. H. Käse, 2001: Synoptic sections of the Denmark Strait overflow. *Geophys. Res. Lett.*, **28**, 1619–1622.
- Jiang, L., and R. W. Garwood Jr., 1996: Three-dimensional simulations of overflows on continental slopes. *J. Phys. Oceanogr.*, **26**, 1214–1233.
- Johnson, G. C., and T. B. Sanford, 1992: Secondary circulation in the Faroe Bank Channel outflow. *J. Phys. Oceanogr.*, **22**, 927–933.
- , R. G. Lueck, and T. B. Sanford, 1994a: Stress on the Mediterranean outflow plume. Part II: Turbulent dissipation and shear measurements. *J. Phys. Oceanogr.*, **24**, 2084–2092.
- , T. B. Sanford, and M. O. Baringer, 1994b: Stress on the Mediterranean outflow plume: Part I. Velocity and water property measurements. *J. Phys. Oceanogr.*, **24**, 2072–2083.
- Jungclaus, J. H., and J. O. Backhaus, 1994: Application of a transient reduced gravity plume model to the Denmark Strait overflow. *J. Geophys. Res.*, **99**, 12 375–12 396.
- , J. Hauser, and R. H. Käse, 2001: Cyclogenesis in the Denmark Strait overflow plume. *J. Phys. Oceanogr.*, **31**, 3214–3229.
- Käse, R. H., and A. Oschlies, 2000: Flow through Denmark Strait. *J. Geophys. Res.*, **105**, 28 527–28 546.
- , J. B. Girton, and T. B. Sanford, 2003: Structure and variability of the Denmark Strait overflow: Model and observations. *J. Geophys. Res.*, in press.
- Killworth, P. D., 1977: Mixing on the Weddell Sea continental slope. *Deep-Sea Res.*, **24**, 427–448.
- , 2001: On the rate of descent of overflows. *J. Geophys. Res.*, **106**, 22 267–22 275.
- , and N. R. Edwards, 1999: A turbulent bottom boundary layer code for use in numerical ocean models. *J. Phys. Oceanogr.*, **29**, 1221–1238.
- Krauss, W., and R. H. Käse, 1998: Eddy formation in the Denmark Strait overflow. *J. Geophys. Res.*, **103**, 15 525–15 538.
- MacCready, P., and P. B. Rhines, 1993: Slippery bottom boundary layers on a slope. *J. Phys. Oceanogr.*, **23**, 5–22.
- Mauritzen, C., 1996: Production of dense overflow waters feeding the North Atlantic across the Greenland–Scotland Ridge. Part 2: An inverse model. *Deep-Sea Res.*, **43A**, 807–835.
- Oakey, N. S., and J. A. Elliott, 1980: The variability of temperature gradient microstructure observed in the Denmark Strait. *J. Geophys. Res.*, **85**, 1933–1944.
- Price, J. F., and M. O. Baringer, 1994: Outflows and deep water production by marginal seas. *Progress in Oceanography*, Vol. 33, Pergamon, 161–200.
- Ross, C. K., 1984: Temperature–salinity characteristics of the “overflow” water in Denmark Strait during “OVERFLOW ’73.” *Rapp. P. V. Reun. Cons. Int. Explor. Mer*, **185**, 111–119.
- Rudels, B., P. Eriksson, H. Grönvall, R. Hietala, and J. Launiainen, 1999: Hydrographic observations in Denmark Strait in fall 1997, and their implications for the entrainment into the overflow plume. *Geophys. Res. Lett.*, **26**, 1325–1328.
- Sanford, T. B., and R.-C. Lien, 1999: Turbulent properties in a homogeneous tidal bottom boundary layer. *J. Geophys. Res.*, **104**, 1245–1257.
- Smith, P. C., 1975: A streamtube model for bottom boundary currents in the ocean. *Deep-Sea Res.*, **22**, 853–873.
- , 1976: Baroclinic instability in the Denmark Strait overflow. *J. Phys. Oceanogr.*, **6**, 355–371.
- Smith, W. H. F., and D. T. Sandwell, 1997: Global sea floor topography from satellite altimetry and ship depth soundings. *Science*, **277**, 1956–1962.
- Stahr, F. R., and T. B. Sanford, 1999: Transport and bottom boundary layer observations of the North Atlantic Deep Western Boundary Current at the Blake Outer Ridge. *Deep-Sea Res.*, **46B**, 205–243.
- Swaters, G. E., 1991: On the baroclinic instability of cold-core coupled density fronts on a sloping continental shelf. *J. Fluid Mech.*, **224**, 361–382.
- Turner, J. S., 1986: Turbulent entrainment: The development of the entrainment assumption, and its application to geophysical flows. *J. Fluid Mech.*, **173**, 431–471.
- Worthington, L. V., 1969: An attempt to measure the volume transport of Norwegian Sea overflow water through the Denmark Strait. *Deep-Sea Res.*, **16**, 421–432.
- Zilitinkevich, S., and D. V. Mironov, 1996: A multi-limit formulation for the equilibrium depth of a stably stratified boundary layer. *Bound.-Layer Meteor.*, **81**, 325–351.



Copyright of Journal of Physical Oceanography is the property of American Meteorological Society and its content may not be copied or emailed to multiple sites or posted to a listserv without the copyright holder's express written permission. However, users may print, download, or email articles for individual use.